PHOTONICS Research

Toward calibration-free Mach–Zehnder switches for next-generation silicon photonics

Lijia Song,[1,2] Tangnan Chen,[1] Weixi Liu,[1] Hongxuan Liu,[1] Yingying Peng,[1] Zejie Yu,[1] Huan Li,[1] Yaocheng Shi,[1] and Daoxin Dai[1,2,*]

[1]State Key Laboratory for Modern Optical Instrumentation, College of Optical Science and Engineering, International Research Center for Advanced Photonics, Zhejiang University, Zijingang Campus, Hangzhou 310058, China
[2]International Research Center for Advanced Photonics, Zhejiang University, Haining 314499, China
*Corresponding author: dxdai@zju.edu.cn

Received 5 November 2021; revised 22 January 2022; accepted 23 January 2022; posted 25 January 2022 (Doc. ID 447478); published 1 March 2022

Silicon photonic Mach–Zehnder switches (MZSs) have been extensively investigated as a promising candidate for optical systems. However, conventional 2 × 2 MZSs are usually prone to the size variations of the arm waveguides due to imperfect fabrication, resulting in considerable random phase imbalance between the two arms, thereby imposing significant challenges for further developing next-generation $N \times N$ MZSs. Here we propose a novel design toward calibration-free 2 × 2 and $N \times N$ MZSs, employing optimally widened arm waveguides, enabled by novel compact tapered Euler S-bends with incorporated mode filters. With standard 180 nm CMOS foundry processes, more than thirty 2 × 2 MZSs and one 4 × 4 Benes MZS with the new design are fabricated and characterized. Compared with their conventional counterparts with 0.45-μm-wide arm waveguides, the present 2 × 2 MZSs exhibit significant reduction in the random phase imbalance. The measured extinction ratios of the present 2 × 2 and 4 × 4 MZSs operating in the all-cross state are 27-49 dB and ∼20 dB across the wavelength range of ∼60 nm, respectively, even without any calibrations. This work paves the way toward calibration-free large-scale $N \times N$ MZSs for next-generation silicon photonics.

https://doi.org/10.1364/PRJ.447478

1. INTRODUCTION

Mach–Zehnder interferometers (MZIs) have been recognized as an indispensable fundamental element in various optical systems due to their great versatility for diverse applications [1–5]. In the past decades, on-chip MZIs have been developed with diverse material systems and have been widely used as one of the most essential components in photonic integrated circuits (PICs) [6–14]. Among them, silicon MZIs are becoming increasingly attractive because silicon photonics features ultrahigh integration density as well as excellent complementary metal-oxide semiconductor (CMOS) compatibility. Silicon MZIs have been developed successfully for realizing variable optical couplers [15,16], optical modulators [17], optical filters [18–21], variable optical attenuators [22], optical sensors [23], and optical switches [24–26]. Among them, Mach–Zehnder switches (MZSs) are one of the most representative functional elements and have been investigated for decades. In particular, thermo-optic (TO) MZSs feature excellent performances and design/fabrication simplicity [27–29], compared to their electro-optic (EO) counterparts based on carrier injection/depletion [24], and, hence, have been extensively investigated as a promising candidate for practical optical interconnects, such as optical burst switching (OBS) in the high-speed optical internet backbone.

Beyond a single 2 × 2 MZS, it is also very important to achieve $N \times N$ MZSs consisting of large-scale networks of 2 × 2 MZSs in cascade. For example, 16 × 16 and 32 × 32 MZSs have been realized on silicon in recent years [30–32]. In this case, the total number of elementary 2 × 2 MZSs scales up rapidly with the port count N, imposing increasingly stringent requirements on the performance of the elementary 2 × 2 MZSs. A typical 2 × 2 MZS is composed of two 2 × 2 3 dB couplers and two symmetric arms, designed for low excess losses and high extinction ratios. However, conventional 2 × 2 MZSs are usually prone to the random size variations of the arm waveguides due to the imperfect fabrication with the state-of-the-art CMOS foundry processes, resulting in considerable accumulated random phase errors and unpredictable phase imbalance between the two arms. In this case, such random phase imbalance must be calibrated and compensated meticulously for all the 2 × 2 MZSs one by one in a large-scale $N \times N$ MZS. Therefore, a large number of additional power taps as well as power monitors are often required for all or part of the 2 × 2 MZS elements, so that the optimal electrical power

for their cross and bar states can be individually determined by monitoring the corresponding tapped power. However, this inevitably introduces significant excess losses. Furthermore, it also entails additional on-chip feedback control schemes and sophisticated characterization procedures, which significantly complicates the layout design and greatly increases the chip footprint as well as the chip management complexity. Besides, it also consumes extra heating power for both cross and bar states. Therefore, it becomes very challenging to scale up $N \times N$ MZSs further. Recently, in Ref. [33], we proposed and demonstrated a new design of 2×2 MZSs with lowered random phase errors for the first time by widening the straight phase-shifter waveguides, which effectively reduced the random phase imbalance, compared to the case of using conventional 0.45-μm-wide single-mode phase-shifters. The fabrication tolerance is, thus, improved, and the power consumption for compensating the phase imbalance is considerably reduced.

Here we propose a novel design toward calibration-free 2×2 and $N \times N$ MZSs that can be mass-manufactured in state-of-the-art silicon photonics foundries. The effective methodology to minimize the size variation sensitivity of the elementary 2×2 MZS is to judiciously widen the entire MZI arm waveguides, including not only the straight phase-shifters but also the S-bends and the tapers, as well as the input/output waveguides of the 2×2 multimode-interference (MMI) couplers. Specifically, the present 2×2 MZS is designed and implemented by introducing novel tapered Euler S-bends (TES-bends) with a widened core width. Furthermore, bent asymmetric directional couplers (ADCs) are incorporated into the TES-bends to filter out residual higher-order modes at the TES-bend entrance. With a standard 180 nm CMOS foundry process, more than thirty 2×2 MZSs with the proposed new design on 11 silicon photonic chips were fabricated and characterized. Compared with those conventional 2×2 MZSs with 0.45-μm-wide single-mode phase-shifters, the present 2×2 MZSs exhibit significant reduction in the random phase imbalance. This validates the improved fabrication tolerance and results in considerable reduction of the power consumption for the phase imbalance compensation. Furthermore, a 4×4 MZS with Benes network topology is also fabricated with the same foundry process and characterized experimentally. The measured extinction ratios of the 2×2 MZS and the 4×4 MZS are 27–49 dB and ~20 dB across a broad wavelength range of ~60 nm, respectively, even without any calibrations. This work paves the way toward calibration-free large-scale $N \times N$ silicon photonic MZSs. The proposed methodology for suppressing the random phase imbalance can be generalized for analog MZI elements and other essential phase-sensitive photonic integrated devices as well, such as micro-rings and arrayed-waveguide gratings (AWGs).

2. DESIGN OF THE ELEMENTARY 2 × 2 MZS

Figure 1(a) shows the schematic configuration of the proposed elementary 2×2 MZS, which consists of two identical 2×2 MMI couplers and two arm waveguides, and Fig. 1(b) shows the cross section of the phase-shifter with a TiN micro-heater on top. Each arm waveguide is composed of a phase-shifter, two adiabatic tapers, two TES-bends, and the straight sections connecting to the input/output ports of the MMI couplers. Here

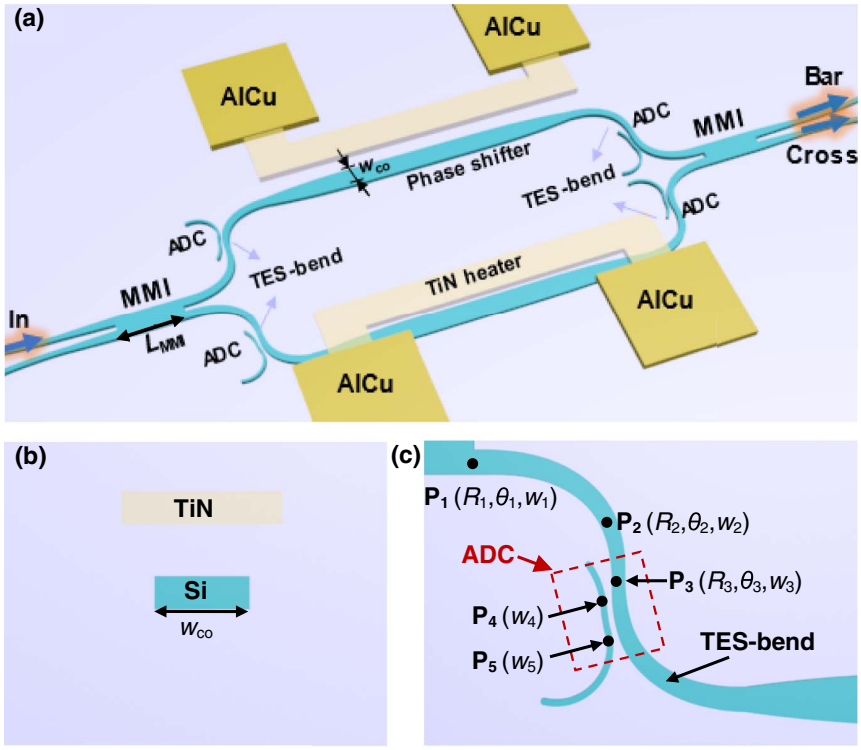

Fig. 1. Schematic configurations of the proposed calibration-free elementary 2×2 MZS. (a) Overview; (b) cross section of the phase-shifter; (c) TES-bend and the bent-ADC mode filter.

the MMI coupler is designed with a 2.4-μm-wide and 20.5-μm-long MMI section, while the width of the input/output waveguides for the MMI coupler is chosen as 0.9 μm. The TES-bends and the widened phase-shifters are connected through ~10 μm-long adiabatic tapers (see Appendix A, Fig. 8).

The S-bends and the phase-shifters of conventional MZSs are usually single-mode, and, thus, their effective indices depend sensitively on the random variation of the core width due to the fabrication errors. Consequently, notable accumulated phase imbalance is usually observed between the two MZS arms due to the random difference in their core widths. A promising solution to this problem is to introduce widened phase-shifters, as proposed in our previous work [33], where the straight section in the phase-shifter is designed to be as wide as 2 μm. One might notice that the S-bends in the MZS arms in Ref. [33] are still as narrow as 450 nm to be single-mode, in order to avoid higher-order mode excitation. Such single-mode S-bends become the dominant contributor to the phase imbalance in the MZS arms.

In contrast, in this paper, it is the first time for incorporating specially designed multimode S-bends into MZSs, whose effective indices are much less dependent on the core width variation. As a result, the random phase imbalances can be greatly reduced. The challenge for such multimode S-bends in an MZS lies in the suppression of higher-order modes when light propagates in the arm waveguides. More specifically, the multimode S-bends should be designed with two key strategies to enable low-loss and low-cross-talk propagation of the fundamental mode. One is to quickly fan out the two waveguides connected with the MMI couplers to avoid any undesired evanescent coupling and thermal cross talk between them. The other is to filter out the residual higher-order modes, especially the dominant TE_1 mode, which is slightly excited with a power ratio of < -15 dB due to imperfect self-imaging at the junction of the input MMI coupler (see Appendix A, Fig. 9). Furthermore, the S-bends should be as compact as possible to reduce the accumulated phase imbalance.

Here a special TES-bend with an incorporated bent-ADC mode filter is introduced, as shown in Fig. 1(c). The TES-bend consists of two identical 90° Euler-bends, whose curvature linearly decreases, with respect to the curve length L, from $1/R_1$ at the end point P_1 (i.e., $\theta = \theta_1$) to $1/R_2$ at the knee point P_2 (i.e., $\theta = \theta_2$), and then linearly increases to $1/R_3$ at the deflection point P_3 (i.e., $\theta = \theta_3$), as shown in Fig. 2(a), where R_1, R_2, and R_3 are the respective curvature radii. Meanwhile, its width varies linearly with respect to the local angle θ, between the width w_1 at the end point P_1, the width w_2 at the knee point P_2, and the width w_3 at the deflection point P_3, as shown in Fig. 2(b). Here the core width w_1 at the end point P_1 ($\theta_1 = 0°$) is chosen as $w_1 = 0.9$ μm to match the MMI coupler input/output ports. Accordingly, the curvature radius R_1 is chosen as $R_1 = 12$ μm to simultaneously minimize the footprint and the mode mismatch between the MMI coupler input/output waveguides and the TES-bend. The core width w_3 and the bending radius R_3 at the deflection point ($\theta_3 = 90°$) are chosen as $w_3 = 0.5$ μm and $R_3 = 10$ μm, respectively, so as to simultaneously minimize the footprint and the mode mismatch between those two sections with opposite curvatures. The other parameters at the knee points are optimally chosen as $\theta_2 = 60°$, $w_2 = 0.67$ μm, and $R_2 = 3$ μm. With this design, the footprint of the TES-bend is as small as ~9 μm × 9 μm.

Figure 3(a) shows the simulated light propagation in the designed TES-bend, where the propagation loss for the TE_0 mode is negligibly low (less than 0.07 dB), while that for the TE_1 mode is much higher (i.e., 1.97 dB) at 1550 nm. To further filter out the residual TE_1 mode, a bent-ADC mode filter is incorporated into the second half of the TES-bend, without increasing the TES-bend footprint, as shown in Fig. 1(c). The bent-ADC mode filter consists of a coupling region where a narrow waveguide is introduced on the convex side near the deflection point of the TES-bend. There is a 0.2-μm-wide gap in the 1.3-μm-long coupling region, and the width of the narrow waveguide varies from 0.24 μm to 0.26 μm (see Appendix A, Fig. 10). In this way, the TE_1 mode in the TES-bend can be coupled out to the TE_0 mode in the narrow waveguide, leading to decent mode filtering within a highly compact footprint. Figure 3(b) shows the simulation results for light propagation of the TE_0 and TE_1 modes with the incorporation of the bent-ADC mode filter, which evidently

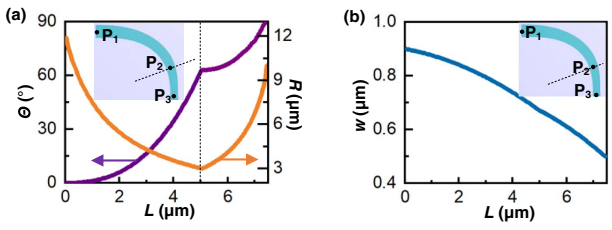

Fig. 2. (a) Local angle θ and the curvature radius R, and (b) the core width w as functions of the curve length L for the first half of the TES-bend.

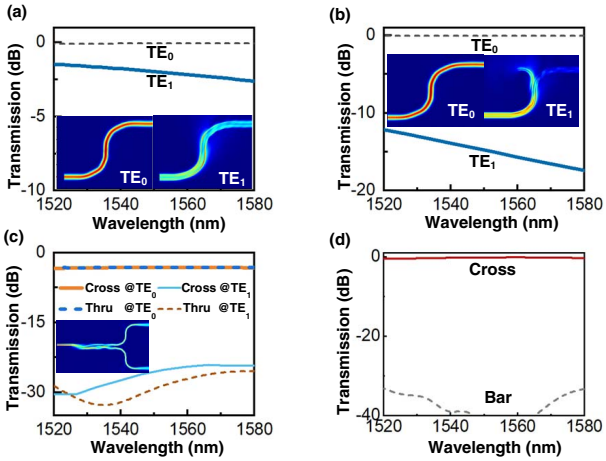

Fig. 3. Simulation results for the designed 2 × 2 MZS. Calculated transmissions of the designed TES-bend (a) without and (b) with the bent-ADC mode filter, respectively. Insets, simulated light propagations when the TE_0 and TE_1 modes are launched, respectively. (c) Calculated transmissions of the MMI coupler connected with the TES-bends. Inset, simulated light propagation for the launched TE_0 mode. (d) Calculated transmissions at the cross and bar ports of the designed MZS in the Off state.

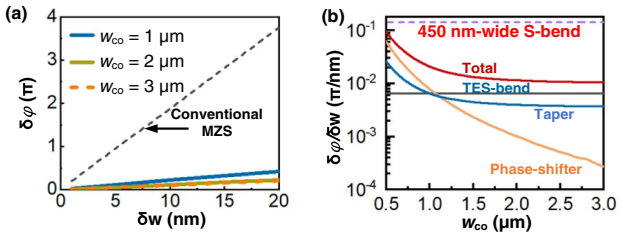

Fig. 4. (a) Calculated total phase imbalance for the new MZS consisting of TES-bends as well as arm waveguides with different core widths of 1, 2, and 3 μm; here the mean width difference δw varies from 1 nm to 20 nm; the result for conventional MZSs with 450-nm-wide arm waveguides is also given; (b) the itemized phase imbalance as the core width w_{co} varies. The results for the conventional MZS with 450-nm-wide S-bends are also included for comparison.

suppresses the TE_1 mode transmission by 12–17 dB, meanwhile introducing negligible transmission loss for the TE_0 mode.

To further validate the TES-bend design, the simulated light propagation through the MMI coupler and the connected TES-bends is shown in Fig. 3(c). It exhibits excellent performances with low non-uniformity of <0.08 dB, low excess loss of ~0.26 dB, and well-suppressed higher-order-mode excitation of < −25 dB in the wavelength range from 1520 nm to 1580 nm. When operating at the central wavelength of 1550 nm, the non-uniformity is about 0.06 dB, the excess loss is ~0.13 dB, and the higher-order mode excitation is < −28 dB. Finally, for the entire MZS consisting of the designed MMI couplers and TES-bends, the transmission spectra at the cross/bar ports are calculated with the finite-difference time-domain (FDTD) method, as shown in Fig. 3(d). It exhibits excellent performances with low excess losses of <0.58 dB and high extinction ratios of ~33 dB in the wavelength range from 1520 nm to 1580 nm.

Figure 4(a) shows the calculated accumulated phase imbalance for the present MZS design as the mean width difference δw varies. In order to provide a quantitative comparison, the result for the conventional MZS is also given. As shown in Fig. 4(a), the designs with the present TES-bends as well as the widened phase-shifter with $w_{co} \geq 2$ μm exhibit ~10-fold lower phase imbalance than the conventional design with $w_{co} = 0.45$ μm. Furthermore, the itemized phase imbalance [33] is analyzed theoretically and shown in Fig. 4(b). It can be seen that the present TES-bend has a lowered phase imbalance of 0.0064π/nm (gray solid line), which is ~22-fold improvement over the conventional 450-nm-wide S-bend (purple dotted line), which is the most representative and widely employed [27,30,33,34]. Note that the TES-bend is still the dominant contributor to the total phase imbalance for the case with ≥2 μm-wide phase-shifters.

3. FABRICATION AND MEASUREMENT

Here the MZSs have been fabricated on silicon-on-insulator (SOI) wafers with a 220-nm-thick top silicon layer and a 2-μm-thick buried oxide (BOX) layer, using standard 180 nm CMOS foundry processes, as shown in Fig. 5(a). Here TiN micro-heaters are on top of both phase-shifters to balance the induced optical loss, if any. Grating couplers are used for convenient and efficient chip-fiber coupling. With the cut-back method, the excess loss of a single TES-bend (with the bent-ADC) has been separately measured to be as low as 0.068 dB [see Appendix A, Fig. 10(c)].

Figures 5(b) and 5(c) show the measurement results for one of the representative MZSs with TES-bends and 2-μm-wide

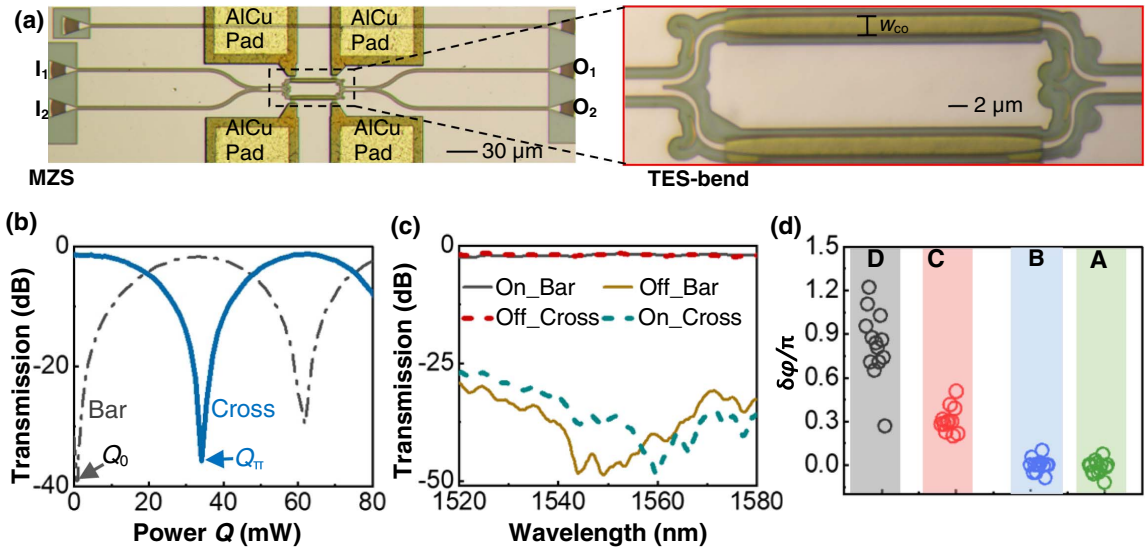

Fig. 5. (a) Optical microscope image of the fabricated 2 × 2 MZS; (b) measured transmissions at the cross/bar ports for the central wavelength when sweeping the heating power Q from 0 to 80 mW; (c) measured transmissions at the cross/bar ports of the present MZS operating at the Off/On (cross/bar) states (i.e., $Q = 0$ and 34 mW, respectively); (d) summary of the measured phase imbalances for all the MZSs (Designs A, B, C, and D) from 11 chips in the same fabrication batch. Design A is with the TES-bends and 2-μm-wide phase-shifters; Design B is with the TES-bends and 1-μm-wide phase-shifters; Design C is with the conventional 0.45-μm-wide S-bends and 2-μm-wide phase-shifters; Design D is with the conventional 0.45-μm-wide S-bends/phase-shifters.

phase-shifters (Design A). From the measured transmissions at the cross/bar ports for the central wavelength when sweeping the heating power from 0 to 80 mW, shown in Fig. 5(b), the phase imbalance is very small, and the corresponding heating power for the compensation is ~0.66 mW only. The bar port has an extinction ratio as high as 32 dB even without any heating power (i.e., $Q = 0$) for phase imbalance compensation. From the transmission spectra at the cross/bar ports of the MZS operating in the Off/On (cross/bar) states (i.e., $Q = 0$ and 34 mW, respectively), the extinction ratios are 27–49 dB in the wavelength range from 1520 nm to 1580 nm. These results verify the excellent performance of the present MZS without any additional power consumption for the phase imbalance compensation, paving the way toward calibration-free MZSs.

To quantify the random phase imbalance $\delta\varphi$ for each MZS device, the cross and bar port transmissions at 1550 nm were measured by sweeping the heating power from 0 to 80 mW. From the measured transmission minima for the bar and cross ports, the heating powers Q_0 and Q_π for the Off- and On-states can be determined, respectively, as shown in Fig. 5(b). Due to the random phase imbalance $\delta\varphi$ for each MZS, usually $Q_0 \neq 0$, as presented in our previous work [33], the TO phase shift $\Delta\varphi$ is proportional to the heating power Q. Consequently, one has $|\delta\varphi|/\pi = Q_0/Q_\pi$. In this way, the phase imbalance $\delta\varphi$ can be calculated from the measured Q_0 and Q_π. Figure 5(d) provides the statistics for the calibrated phase imbalances $\delta\varphi$ for all the MZSs on our 11 chips diced from the same SOI wafer. There are four types of MZSs, including Design A described above, Design B with the TES-bends and 1-μm-wide phase-shifters, Design C with the conventional 0.45-μm-wide S-bends and 2-μm-wide phase-shifters, and Design D with the conventional 0.45-μm-wide S-bends/phase-shifters. As shown in Fig. 5(d), for Design D (i.e., the conventional design), the mean and standard deviation of the phase imbalance are 0.70π and 0.50π, respectively, denoted as $(0.70 \pm 0.50)\pi$ for short in the following. Such large random phase imbalances must be calibrated and compensated carefully when the MZS is used. In contrast, when the phase-shifter is broadened to 2 μm, the random phase imbalance for Design C (with 0.45-μm S-bends and 2-μm-wide phase-shifters) is reduced greatly to be $(0.31 \pm 0.08)\pi$. When the S-bends are also broadened by introducing the TES-bend design, Design A (with TES-bends and 2-μm-wide phase-shifters) has a phase imbalance reduced further to $(0.016 \pm 0.045)\pi$, which indicates the phase imbalance can be reduced greatly by incorporating TES-bends into MZSs. For Designs B with the present TES-bends and 1-μm-wide phase-shifters, the phase imbalance is also very low, i.e., $(0.0019 \pm 0.077)\pi$, as expected. The comparison between Designs A and B indicates that the random variation of the phase-shifters does not contribute dominantly to the phase imbalance when the core width is wider than 1 μm, consistent with the theoretical calculations in Fig. 4(b). As a summary, for Designs A and B, the superior performances with high extinction ratios and low excess losses are achieved even without any calibration for the Off state, as shown in Fig. 5(d). This promises to greatly simplify the calibration particularly for $N \times N$ MZSs with a large number of 2×2 MZSs, as well as to reduce the power consumption significantly for phase-imbalance compensation.

The present 2×2 MZS with Design A is used further for the realization of a 4×4 MZS with Benes network, which consists of six 2×2 MZSs cascaded in three stages, as shown in Fig. 6(a). Here we only present the measured transmission spectra from the most representative switching states, i.e., all-cross, all-bar, and the six single-bar switching states (see Appendix A, Fig. 11). When the 4×4 MZS operates in the all-cross state, the signals launched from input ports I_1, I_2,

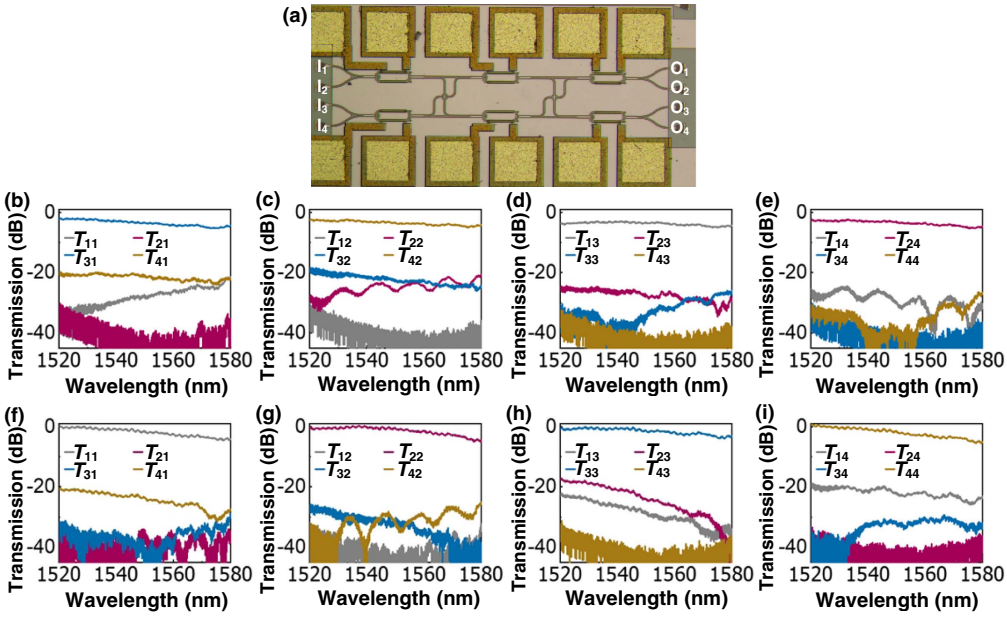

Fig. 6. (a) Optical microscope image, and (b)–(e) measured all-cross transmissions T_{ij} at the output port O_j with the port I_i importing when $i = 1, 2, 3$, and 4, respectively, with no calibration for all the six MZSs. (f)–(i) Measured all-bar transmissions T_{ij}, where the signals launched from input ports I_1, I_2, I_3, and I_4 are routed to output ports O_1, O_2, O_3, and O_4, respectively.

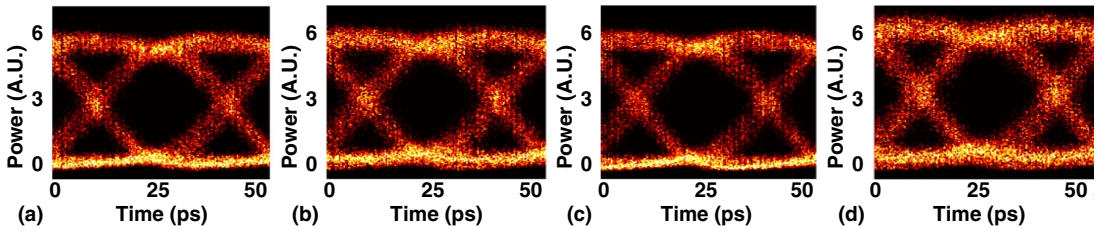

Fig. 7. Synthesized eye-diagrams at port (a) O_1, (b) O_2, (c) O_3, and (d) O_4 of the present 4 × 4 MZS in the all-cross states. Here the bit rate is 30 Gb/s.

I_3, and I_4 are routed to output ports O_3, O_4, O_1, and O_2, respectively. Figures 6(b)–6(e) show the measured all-cross transmission spectra T_{ij} at the output port O_j from the input port I_i when $i = 1, 2, 3$, and 4, respectively, with no calibration for any of the six MZSs (i.e., the powers applied to the six micro-heaters are zero). The extinction ratios for all the ports are ∼20 dB across the 60 nm wavelength range. The extinction ratio for the 4 × 4 MZS is lower than the 2 × 2 MZS due to the accumulated cross talk of all the paths [35]. When the 4 × 4 MZS operates in the all-bar state, the signals launched from input ports I_1, I_2, I_3, and I_4 are routed to output ports O_1, O_2, O_3, and O_4, respectively. Figures 6(f)–6(i) show the measured all-bar transmission spectra T_{ij} defined above, exhibiting excellent performances similar to the cases with all-cross states.

The 4 × 4 MZS is further used to demonstrate high-bit-rate data routing. In order to characterize the signal integrity degradation due to the MZS cross talk, eye-diagrams at any output port O_j should be recorded when all four data channels are launched into the input ports I_i ($i = 1$, 2, 3, and 4). However, due to the lack of concurrent data generators in the lab, we synthesize the eye-diagrams at the output port O_j from the measured transmissions T_{ij} by reasonably assuming the four inputs are incoherent. In our experiments, the 30 Gb/s non-return-to-zero (NRZ) data were launched into the input ports one by one, and the transmissions T_{ij} from input port I_i to output port O_j were measured and recorded. The eye-diagram T_j at the output port O_j is synthesized by summing the transmissions T_{ij} ($i = 1$, 2, 3, and 4), i.e., $T_j = \sum_i T_{ij}$. Figures 7(a)–7(d) show the synthesized eye-diagrams for ports O_1, O_2, O_3, and O_4, respectively, exhibiting open eye-diagrams with high signal-to-noise ratios, which validates the high-bit-rate data routing of the present 4 × 4 MZS in the all-cross states.

4. CONCLUSION

Our theoretical analysis and experimental results above, especially the statistical comparison between our new MZS designs and the conventional one on the chips diced from the same SOI wafer, unambiguously confirm the effectiveness of our methodology to reduce the random phase imbalance. The present calibration-free 4 × 4 Benes MZS already shows promising results that are sufficient for certain practical applications, which is an important first step toward large-scale calibration-free MZSs on silicon. More generally, excellent fabrication tolerance is an important premise that must be achieved to enable the further scaling of silicon photonic circuits, which is becoming the consensus of the silicon photonics community. We believe this work is an important breakthrough to meet the challenge of fabrication tolerance, which is currently a major hinderance for the real-world mass deployment of silicon photonic devices, especially the large-scale passive devices.

In conclusion, we have proposed a novel design toward calibration-free 2 × 2 and $N \times N$ MZSs that can be mass-manufactured in state-of-the-art silicon photonics foundries by judiciously widening the MZI arm waveguides. Specifically, the present 2 × 2 MZS is designed and implemented by introducing novel TES-bends with a widened core width and incorporated bent-ADC mode filters. With a standard 180 nm CMOS foundry process, more than thirty 2 × 2 MZSs and one 4 × 4 Benes MZS with the new design have been fabricated and characterized. Compared with those conventional 2 × 2 MZSs with 0.45-μm-wide single-mode phase-shifters, the present 2 × 2 MZSs with 2-μm-wide phase-shifters exhibit a significantly suppressed random phase imbalance of $(0.016 \pm 0.045)\pi$. The fabricated 2 × 2 and 4 × 4 MZSs feature high extinction ratios of 27–49 dB and ∼20 dB across a ∼60 nm wavelength range, respectively, even without any calibrations. These results pave the way toward large-scale calibration-free $N \times N$ silicon photonic MZSs while more effort should be made to prevent the extinction ratio from deteriorating due to the accumulated cross talk from all the paths. The proposed methodology for suppressing the random phase imbalance can be generalized for analog MZI elements and other essential phase-sensitive integrated photonic elements as well, such as micro-rings and AWGs. This is extremely attractive for developing next-generation silicon PICs with many elements as well as simplified calibrations.

APPENDIX A

In this work, we optimized the taper with compact nonlinear curves to achieve low excess loss and a widened core width to minimize the random phase error. For the 10-μm-long tapers considered here, different taper shapes have been introduced. The excess loss of the TE_0 mode and the mode excitation ratio to the TE_1 mode are calculated, and the corresponding results are shown in Fig. 8, which suggests that the quadratic taper is the optimal design with the excess loss of <0.013 dB and the mode excitation ratio < − 36 dB in theory across the wavelength range from 1520 nm to 1580 nm.

Here the MMI coupler is designed with a 2.4-μm-wide and 20.5-μm-long MMI section, while the width of the input/output waveguides for the MMI coupler is chosen as 0.9 μm.

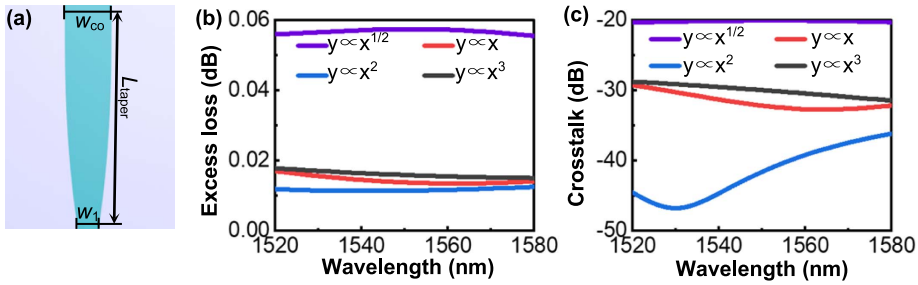

Fig. 8. Adiabatic taper with different shapes. (a) Structure. (b) Calculated excess loss for the TE_0 mode. (c) Calculated mode excitation ratio to the TE_1 mode. Here $w_{co} = 2$ μm and $w_1 = 0.9$ μm.

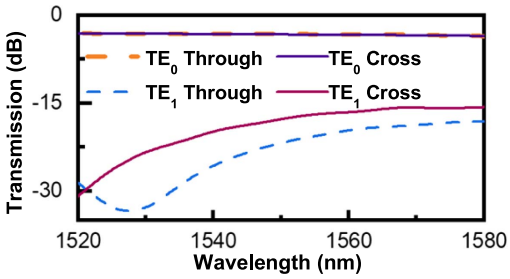

Fig. 9. Simulated transmission spectra of the 2 × 2 MMI coupler, including the TE_0 and TE_1 modes at the cross and through ports.

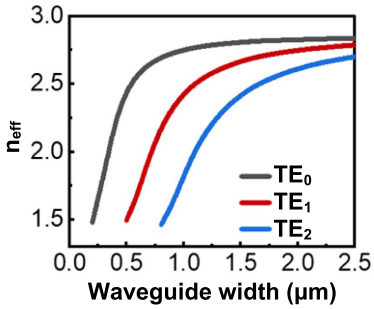

Fig. 10. Calculated effective indices of the TE modes of 220-nm-thick silicon waveguides.

Figure 9 shows the simulated transmissions of the designed 2 × 2 MMI coupler, including the TE_0 and TE_1 modes at the cross and through ports, exhibiting low non-uniformity of <0.1 dB, excess losses of 0.24 dB for the TE_0 mode, and low excitation ratios of < −15 dB for the TE_1 modes due to imperfect self-imaging. The residual TE_1 modes are further suppressed with the bent-ADC mode filters in the TES-bends.

Figure 10 shows the effective indices of the TE modes of 220-nm-thick silicon waveguides as the core width w_{co} varies. According to the coupled-mode theory, the higher-order mode (TE_1) in the TES-bend evolves to the fundamental mode (TE_0) in the narrow waveguide, whose width varies from 0.24 μm to 0.26 μm to follow the width change of the TES-bend.

To characterize the excess loss of the TES-bend (with the bent-ADC), we designed and fabricated the test structures with 10, 18, 48, and 98 identical TES-bends in cascade, as shown in Figs. 11(a) and 11(b). Figure 11(c) shows the measured transmissions for these samples. It can be seen that the measured excess loss of a single TES-bend is about 0.068 dB, which agrees well with the simulated value of 0.069 dB.

Figure 12 shows the measured transmission spectra from the six single-bar switching states for the fabricated 4 × 4 MZS, i.e., (10|00|00), (01|00|00), (00|10|00), (00|01|00), (00|00|10), and (00|00|01), respectively. Here the digits 0 and 1 stand for the cross and bar states of the MZSs, which are grouped into stages and delimited by the symbol "|". The on-chip excess loss is ∼1.5 dB at 1550 nm and the extinction ratio is ∼20 dB across the ∼60 nm bandwidth.

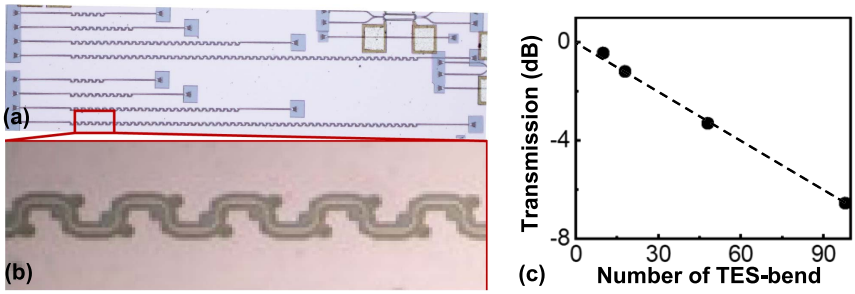

Fig. 11. (a), (b) Optical microscope images of TES-bend. (c) The measured transmissions for the testing structures with a number of TES-bends in cascade.

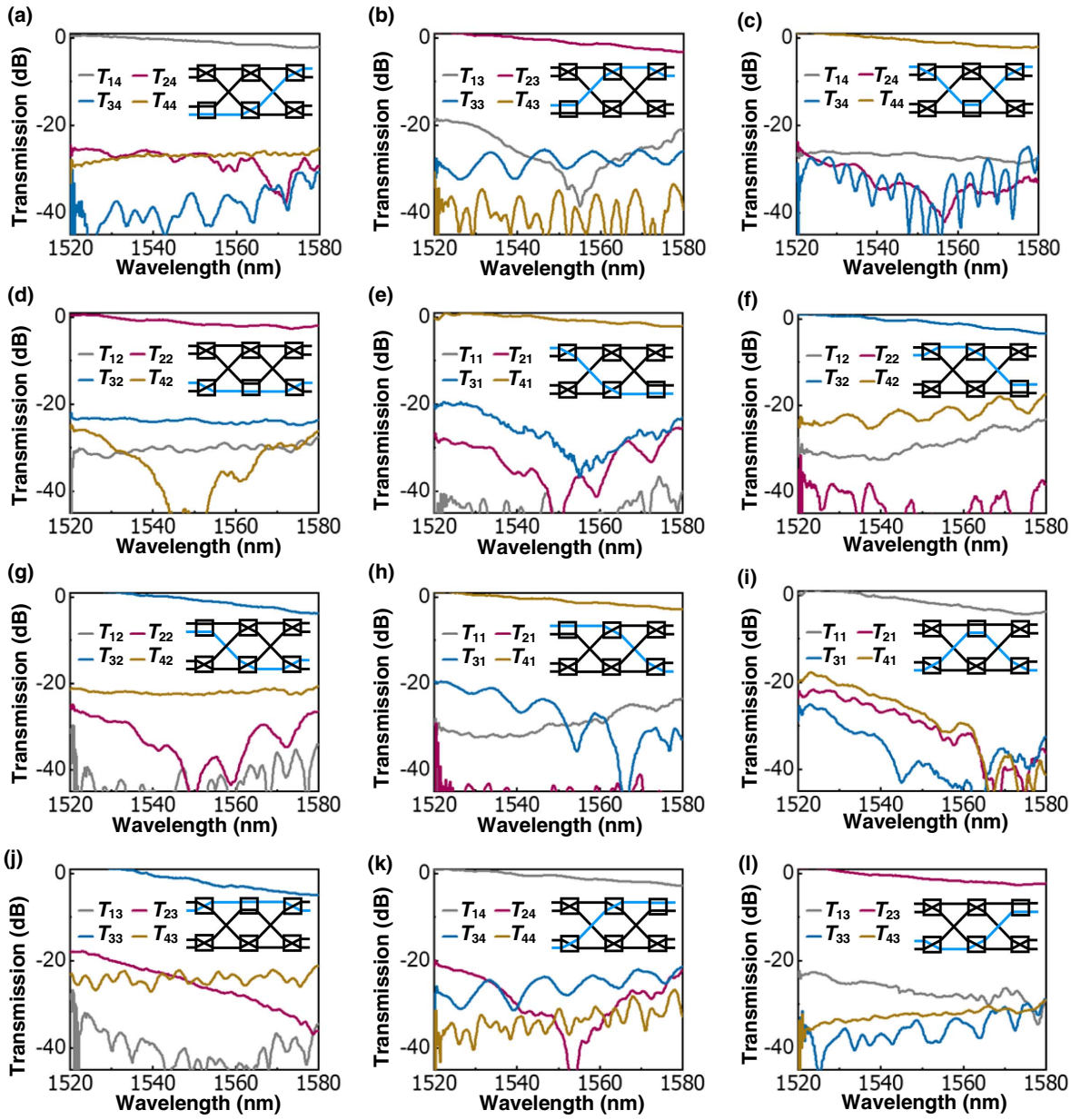

Fig. 12. Measured transmissions of the fabricated 4 × 4 MZS with Benes network in (a), (b) (10|00|00) state; (c), (d) (01|00|00) state; (e), (f) (00|10|00) state; (g), (h) (00|01|00) state; (i), (j) (00|00|10) state; (k), (l) (00|00|01) state.

Funding. National Key Research and Development Program of China (2019YFB2203603); Zhejiang Provincial Major Research and Development Program (2021C01199); National Science Fund for Distinguished Young Scholars (61725503); National Natural Science Foundation of China (61961146003, 91950205); Zhejiang Provincial Natural Science Foundation (LD19F050001, LZ18F050001); Fundamental Research Funds for the Central Universities (2021QNA5002).

Disclosures. The authors declare no conflicts of interest.

Data Availability. Data underlying the results presented in this paper are not publicly available at this time but may be obtained from the authors upon reasonable request.

REFERENCES

1. Y. Li and L. Tong, "Mach–Zehnder interferometers assembled with optical microfibers or nanofibers," Opt. Lett. **33**, 303–305 (2008).
2. D. A. B. Miller, "Perfect optics with imperfect components," Optica **2**, 747–750 (2015).
3. Y. Zhang, Q. Du, C. Wang, T. Fakhrul, S. Liu, L. Deng, D. Huang, P. Pintus, J. Bowers, C. A. Ross, J. Hu, and L. Bi, "Monolithic integration of broadband optical isolators for polarization-diverse silicon photonics," Optica **6**, 473–478 (2019).
4. S. Ghosh, S. Keyvaninia, Y. Shoji, W. Roy, T. Mizumoto, G. Roelkens, and R. Baets, "Compact Mach–Zehnder interferometer Ce:YIG/SOI optical isolators," IEEE Photon. Technol. Lett. **24**, 1653–1656 (2012).
5. C. Zhang, P. Morton, J. Khurgin, J. Peters, and J. Bowers, "Ultralinear heterogeneously integrated ring-assisted Mach–Zehnder interferometer modulator on silicon," Optica **3**, 1483–1488 (2016).

6. A. M. Al-Hetar, A. B. Mohammad, A. S. M. Supaat, and Z. A. Shamsan, "MMI-MZI polymer thermo-optic switch with a high refractive index contrast," J. Lightwave Technol. **29**, 171–178 (2011).
7. M. He, M. Xu, Y. Ren, J. Jian, Z. Ruan, Y. Xu, S. Gao, S. Sun, X. Wen, L. Zhou, L. Liu, C. Guo, H. Chen, S. Yu, L. Liu, and X. Cai, "High-performance hybrid silicon and lithium niobate Mach–Zehnder modulators for 100 Gbit s^{-1} and beyond," Nat. Photonics **13**, 359–364 (2019).
8. A. Ribeiro, A. Ruocco, L. Vanacker, and W. Bogaerts, "Demonstration of a 4 × 4-port universal linear circuit," Optica **3**, 1348–1357 (2016).
9. J. S. Barton, E. J. Skogen, M. L. Masanovic, S. P. Denbaars, and L. A. Coldren, "A widely tunable high-speed transmitter using an integrated SGDBR laser-semiconductor optical amplifier and Mach-Zehnder modulator," IEEE J. Sel. Top. Quantum Electron. **9**, 1113–1117 (2003).
10. R. Amin, R. Maiti, Y. Gui, C. Suer, M. Miscuglio, E. Heidari, R. T. Chen, H. Dalir, and V. J. Sorger, "Sub-wavelength GHz-fast broadband ITO Mach–Zehnder modulator on silicon photonics," Optica **7**, 333–335 (2020).
11. H. Wang, H. Chai, Z. Lv, Z. Zhang, L. Meng, X. Yang, and T. Yang, "Silicon photonic transceivers for application in data centers," J. Semicond. **41**, 101301 (2020).
12. P. Bhasker, J. Norman, J. Bowers, and N. Dagli, "Intensity and phase modulators at 1.55 μm in GaAs/AlGaAs layers directly grown on silicon," J. Lightwave Technol. **36**, 4205–4210 (2018).
13. D. Korn, R. Palmer, and H. Yu*et al.*et al., "Silicon-organic hybrid (SOH) IQ modulator using the linear electro-optic effect for transmitting 16QAM at 112 Gbit/s," Opt. Express **21**, 13219–13227 (2013).
14. X. Yang, M. S. Nisar, W. Yuan, F. Zheng, L. Lu, J. Chen, and L. Zhou, "Phase change material enabled 2 × 2 silicon nonvolatile optical switch," Opt. Lett. **46**, 4224–4227 (2021).
15. W. R. Clements, P. C. Humphreys, B. J. Metcalf, W. S. Kolthammer, and I. A. Walmsley, "Optimal design for universal multiport interferometers," Optica **3**, 1460–1465 (2016).
16. M. Reck, A. Zeilinger, H. J. Bernstein, and P. Bertani, "Experimental realization of any discrete unitary operator," Phys. Rev. Lett. **73**, 58–61 (1994).
17. A. Liu, R. Jones, L. Liao, D. Samara-Rubio, D. Rubin, O. Cohen, R. Nicolaescu, and M. Paniccia, "A high-speed silicon optical modulator based on a metal–oxide–semiconductor capacitor," Nature **427**, 615–618 (2004).
18. R. A. Soref, F. De Leonardis, and V. M. N. Passaro, "Reconfigurable optical-microwave filter banks using thermo-optically tuned Bragg Mach-Zehnder devices," Opt. Express **26**, 14879–14893 (2018).
19. F. Horst, W. M. J. Green, S. Assefa, S. M. Shank, Y. A. Vlasov, and B. J. Offrein, "Cascaded Mach-Zehnder wavelength filters in silicon photonics for low loss and flat pass-band WDM (de-)multiplexing," Opt. Express **21**, 11652–11658 (2013).
20. M. E. Ganbold, H. Nagai, Y. Mori, K. Suzuki, H. Matsuura, K. Tanizawa, K. Ikeda, S. Namiki, H. Kawashima, and K. I. Sato, "A large-scale optical circuit switch using fast wavelength-tunable and bandwidth-variable filters," IEEE Photon. Technol. Lett. **30**, 1439–1442 (2018).
21. L. Shen, L. Lu, Z. Guo, L. Zhou, and J. Chen, "Silicon optical filters reconfigured from a 16 × 16 Benes switch matrix," Opt. Express **27**, 16945–16957 (2019).
22. Q. Wu, L. Zhou, X. Sun, H. Zhu, L. Lu, and J. Chen, "Silicon thermo-optic variable optical attenuators based on Mach–Zehnder interference structures," Opt. Commun. **341**, 69–73 (2015).
23. K. Misiakos, I. Raptis, E. Makarona, A. Botsialas, A. Salapatas, P. Oikonomou, A. Psarouli, P. S. Petrou, S. E. Kakabakos, K. Tukkiniemi, M. Sopanen, and G. Jobst, "All-silicon monolithic Mach-Zehnder interferometer as a refractive index and bio-chemical sensor," Opt. Express **22**, 26803–26813 (2014).
24. M. Yang, W. M. J. Green, S. Assefa, J. Van Campenhout, B. G. Lee, C. V. Jahnes, F. E. Doany, C. L. Schow, J. A. Kash, and Y. A. Vlasov, "Non-blocking 4 × 4 electro-optic silicon switch for on-chip photonic networks," Opt. Express **19**, 47–54 (2011).
25. N. Dupuis, A. V. Rylyakov, C. L. Schow, D. M. Kuchta, C. W. Baks, J. S. Orcutt, D. M. Gill, W. M. J. Green, and B. G. Lee, "Ultralow crosstalk nanosecond-scale nested 2 × 2 Mach–Zehnder silicon photonic switch," Opt. Lett. **41**, 3002–3005 (2016).
26. K. Suzuki, R. Konoike, G. Cong, K. Yamada, S. Namiki, H. Kawashima, and K. Ikeda, "Strictly non-blocking 8 × 8 silicon photonics switch operating in the O-band," J. Lightwave Technol. **39**, 1096–1101 (2021).
27. S. Wang and D. Dai, "Polarization-insensitive 2 × 2 thermo-optic Mach-Zehnder switch on silicon," Opt. Lett. **43**, 2531–2534 (2018).
28. F. Duan, K. Chen, D. Chen, and Y. Yu, "Low-power and high-speed 2 × 2 thermo-optic MMI-MZI switch with suspended phase arms and heater-on-slab structure," Opt. Lett. **46**, 234–237 (2021).
29. L. Chen and Y.-K. Chen, "Compact, low-loss and low-power 8 × 8 broadband silicon optical switch," Opt. Express **20**, 18977–18985 (2012).
30. S. Zhao, L. Lu, L. Zhou, D. Li, Z. Guo, and J. Chen, "16 × 16 silicon Mach–Zehnder interferometer switch actuated with waveguide microheaters," Photon. Res. **4**, 202–207 (2016).
31. L. Qiao, W. Tang, and T. Chu, "32 × 32 silicon electro-optic switch with built-in monitors and balanced-status units," Sci. Rep. **7**, 42306 (2017).
32. K. Tanizawa, K. Suzuki, M. Toyama, M. Ohtsuka, N. Yokoyama, K. Matsumaro, M. Seki, K. Koshino, T. Sugaya, S. Suda, G. Cong, T. Kimura, K. Ikeda, S. Namiki, and H. Kawashima, "Ultra-compact 32 × 32 strictly-non-blocking Si-wire optical switch with fan-out LGA interposer," Opt. Express **23**, 17599–17606 (2015).
33. L. Song, H. Li, and D. Dai, "Mach–Zehnder silicon-photonic switch with low random phase errors," Opt. Lett. **46**, 78–81 (2021).
34. K. Suzuki, G. Cong, K. Tanizawa, S.-H. Kim, K. Ikeda, S. Namiki, and H. Kawashima, "Ultra-high-extinction-ratio 2 × 2 silicon optical switch with variable splitter," Opt. Express **23**, 9086–9092 (2015).
35. N. Dupuis and B. G. Lee, "Impact of topology on the scalability of Mach–Zehnder-based multistage silicon photonic switch networks," J. Lightwave Technol. **36**, 763–772 (2018).